Astron. Astrophys. 337, 421–432 (1998)

ASTRONOMY AND ASTROPHYSICS

Detection of pulsed MeV emission from PSR B1951+32 by COMPTEL

L. Kuiper[2], W. Hermsen[2], K. Bennett[4], A. Carramiñana[5], A. Lyne[6], M. McConnell[3], and V. Schönfelder[1]

[1] Max-Planck Institut für Extraterrestrische Physik, D-8046 Garching, Germany
[2] SRON-Utrecht, Sorbonnelaan 2, 3584 CA Utrecht, The Netherlands
[3] Space Science Centre, University of New Hampshire, Durham, NH 03824, USA
[4] Astrophysics Division, European Space Research and Technology Centre, 2200 AG Noordwijk, The Netherlands
[5] I.N.A.O.E., Apartado Postal 51 y 216, Puebla 72000, Puebla, México
[6] University of Manchester, NRAL, Jodrell Bank, Cheshire SK11 9DL, UK

Received 23 January 1998 / Accepted 3 June 1998

Abstract. We report on the detection at MeV energies of the radio pulsar PSR B1951+32 by the Compton telescope COMPTEL aboard the COMPTON Gamma Ray Observatory (CGRO). Folding the event arrival times with the radio ephemerides, gives for the data collected during CGRO-mission Cycles I+II a pulsar-phase distribution with two peaks, consistent in phase with the pulses measured by EGRET for energies above 100 MeV. The overall significance is $\gtrsim 4.1\sigma$. For Cycle III-VI data, with similar exposure, no indication was found in the phase distribution. Assuming that the source is not variable, simulations show that fluctuations in the dominating background distribution at significance levels $\lesssim 3\sigma$ can explain the non-detection. In addition, evidence for the presence of the pulsar in the skymaps for energies above 3 MeV is found for all Cycles of the CGRO mission. Below 3 MeV the skymaps are dominated by the strong, soft-spectrum gamma-ray source Cyg X-1, located at only $\sim 2\overset{\circ}{.}6$ from PSR B1951+32. The flux $(7.7 \pm 4.6) \times 10^{-7}\ ph/cm^2 \cdot s \cdot MeV$ measured by COMPTEL between 0.75 and 30 MeV is consistent with the measured EGRET spectrum. A single power-law fit to the combined EGRET–COMPTEL data (0.75 MeV – 30 GeV) gives an good fit with spectral index -1.89 ± 0.07. Furthermore, a break in the pulsar spectrum at MeV energies appears to be required to reconcile the COMPTEL flux with upper limits reported below 1 MeV by OSSE and RXTE.

Key words: gamma rays: observations – pulsars: individual: PSR B1951+32

1. Introduction

Kulkarni et al. (1988) discovered PSR B1951+32, a fast 39.5 ms radio-pulsar in the core of the galactic supernova remnant CTB 80 (Angerhofer et al. 1981). The characteristic age and surface field strength assuming spin-down by magnetic dipole radiation are 1.1×10^5 yr and 5×10^{11} Gauss respectively (Fruchter et al. 1988). Its distance based on both pulsar dispersion measure and estimates of the distance to the remnant is ~ 2 kpc.

In the X-ray regime marginal detections of pulsed emission were claimed by Ögelman et al. (1987) and Angelini et al. (1988) in the EXOSAT data and by Cheng et al. (1994) in the *Einstein* data. Safi-Harb et al. (1995) published detailed results on the soft X-ray properties of PSR B1951+32 and CTB 80 using the ROSAT PSPC and HRI instruments. A combination of PSPC and HRI data yielded marginal evidence at a $\sim 99\%$ confidence level for pulsed emission at the radio period. Recently, at hard X-ray energies Chang et al. (1997) found indications for pulsed emission at $\sim 95\%$ confidence level in a 19 ks observation with the PCA aboard the Rossi X-ray timing explorer (RXTE).

Extrapolating the pulsar ephemeris (Fruchter et al. 1988, Foster et al. 1990, 1994) backwards, timing analysis of COS-B γ-ray data (E$>$ 50 MeV) yielded promising results (Li et al. 1990; Bennett et al. 1990).

Using γ-ray observations by the EGRET instrument aboard the COMPTON Gamma-Ray Observatory (CGRO) Ramanamurthy et al. (1995) firmly detected pulsed emission from PSR B1951+32 for energies above 100 MeV. The lightcurve showed 2 peaks separated 0.44 in phase with the first peak lagging the radio peak by 0.16. In an earlier systematic search for pulsed γ-ray emission from radio pulsars in CGRO Cycle I COMPTEL data ($0.75 - 30$ MeV) Carramiñana et al. (1995) found indications (random probability 0.62%) for a double-peak structure in the lightcurve, but had no information on the absolute phase.

In this paper we report now on the detection of PSR B1951+32 by COMPTEL using more data and absolute timing, and the results are compared with those from simultaneous EGRET observations. Preliminary results from this work were presented by Hermsen et al. (1997).

2. Observations

In this study we have used COMPTEL data collected during CGRO Cycle I - VI observations in which the off-axis angle between PSR B1951+32 located at (*l*,*b*) $= (68\overset{\circ}{.}77, 2\overset{\circ}{.}82)$ and the pointing direction was less than 30°. Details of each viewing period (VP, in CGRO notation) satisfying the aspect angle

Send offprint requests to: e-mail: L.Kuiper@sron.ruu.nl

Table 1. COMPTEL observations of PSR B1951+32

VP #	Start Date dd-mm-yyyy	End Date dd-mm-yyyy	Pointing direction l(°)	b(°)	Off-axis angle (°)	Eff.Exposure (3-10 MeV; $10^6\ cm^2 s$)	EGRET spark-chamber status
Cycle I							
2.0	30-05-1991	08-06-1991	73.3	2.5	4.5	7.927	ON
7.0	08-08-1991	15-08-1991	70.5	-8.4	11.3	5.237	ON
20	06-02-1992	20-02-1992	39.8	0.7	29.1	4.853	ON
Cycle II							
203.0	01-12-1992	08-12-1992	77.8	0.7	9.3	$\top$	ON
203.3	08-12-1992	15-12-1992	77.8	0.7	9.3	16.435	ON
203.6	15-12-1992	22-12-1992	77.8	0.7	9.3	$\perp$	ON
212	09-03-1993	23-03-1993	83.7	11.7	17.2	8.516	ON
Cycle III							
302.0	07-09-1993	09-09-1993	89.1	7.9	20.8	$\top$	ON
303.2	22-09-1993	01-10-1993	89.1	7.9	20.8	3.717	ON
303.7	18-10-1993	19-10-1993	89.1	7.8	20.8	$\perp$	ON
318	01-02-1994	08-02-1994	68.4	-0.4	3.3	$\top$	ON
328	24-05-1994	31-05-1994	64.9	0.0	4.8	11.247	ON
331.0	07-06-1994	10-06-1994	64.9	0.0	4.8	$\perp$	ON
331.5	14-06-1994	18-06-1994	64.9	0.0	4.8	2.948	ON
333	05-07-1994	12-07-1994	64.9	0.0	4.8	4.520	ON
Cycle IV							
429.5	27-09-1995	03-10-1995	86.3	-12.6	23.2	2.798	OFF
Cycle V							
522.5	14-06-1996	25-06-1996	65.7	2.8	3.1	8.064	OFF
Cycle VI							
601.1	15-10-1996	29-10-1996	69.7	-11.3	14.2	8.344	ON
612.5	28-01-1997	04-02-1997	71.3	3.1	2.6	5.204	OFF

constraint are given in Table 1. In this paper we depart from the official CGRO nomenclature by using Cycle I - VI instead of the confusing mixture of Phases and Cycles.

The last but one column gives the effective exposure in the 3-10 MeV band at the location of PSR B1951+32 assuming an E^{-2} power-law shape for the spectral distribution of the source events. Earth blocking effects are taken into account. Time periods in which the instrument detectors are off (e.g. anticipated during CGRO SAA passages) and in which there is no real time contact with the TDRS satellites are ignored in this calculation. The last column specifies the status of the EGRET sparkchamber, which is turned off regularly as of CGRO Cycle-IV observations in order to use the last refill of deteriorating gas for more restrictive observations spread over a longer time period. This means that there are no simultaneous EGRET observations for VP's 429.5, 522.5 and 612.5. EGRET data from VP 2.0 upto and including VP 333 have been retrieved from the Compton Science Support Center and used subsequently in our timing- and spatial analysis for verification purposes.

3. The COMPTEL instrument

COMPTEL is the imaging Compton Telescope aboard CGRO and is sensitive for γ-ray photons with energies in the 0.75-30 MeV range. Its energy resolution is 5-10% FWHM and due to its large field of view of typically 1 steradian it is possible to monitor a large part of the sky simultaneously with a location resolution of $\sim 1^\circ$. Its event-timing accuracy is 0.125 ms.

The COMPTEL instrument consists of two detector layers, an upper layer (D1) and a lower layer (D2). Its detection principle is based on a two layer interaction : an incoming γ-ray photon Compton scatters in one of the 7 detector modules of D1, while the scattered photon has another interaction in one of the 14 D2 modules. The interaction loci in D1 and D2 determine the direction of the scattered photon, which is specified as (χ, ψ). From the energy deposits in the D1 - module, E_1, and D2- module, E_2, it is possible to determine the scatter angle $\overline{\varphi}$ $(= \arccos(1 - m_0c^2(1/E_1 - 1/(E_1 + E_2)))$, in which m_0c^2 is the electron rest energy) and the total energy deposit E_{tot} $(= E_1 + E_2)$. Other event parameters playing an important role in background discrimination are: The four Veto Domes anti-coincidence bits enabling the filtering of the charged particle triggers from the neutral particle triggers at efficiencies above 99.9%; The Time-of-Flight (TOF) measure (range 0-255) for which down-scattered γ-ray photons have well-defined values in a Gaussian shaped peak near channel 120; The Pulse-Shape-Discrimination (PSD) measure (range 0-255) of the signal built up in one of the 7 D1 detectors allowing further discrimination among photon- and neutron induced triggers (photons peak near channel 80, while neutrons peak near 120). In the

Table 2. PSR B1951+32 radio-ephemerides used in current analysis

Pulsar position		Validity range		t^0	ν	$\dot{\nu}$	$\ddot{\nu}$	ϕ_0
α_{2000}	δ_{2000}	[MJD]		[MJD]	[Hz]	[Hz/s]	[Hz/s^2]	
19 52 58.322	32 52 41.88	48350	48678	48514[a]	25.296909436979	-3.74070×10^{-12}	3.34×10^{-22}	0.7381
19 52 58.242	32 52 40.96	48898	49099	48998[b]	25.2967530149361	-3.74216×10^{-12}	0.0	0.7103
19 52 58.242	32 52 40.96	49217	49574	49395[c]	25.2966246804332	-3.74149×10^{-12}	-5.89×10^{-23}	0.8769
19 52 58.276	32 52 40.68	49954	50207	50080[c]	25.2964033322986	-3.73751×10^{-12}	-6.18×10^{-22}	0.1300
19 52 58.276	32 52 40.68	50232	50513	50372[c]	25.2963090136230	-3.73684×10^{-12}	-2.64×10^{-23}	0.7351

[a] Entry from Princeton Database (Cordes et al. 1992)
[b] Entry listed in Ramanamurthy et al. 1995
[c] Provided by A.Lyne

event selection process also events which may originate from the Earth are ignored (Earth Horizon Angle (EHA) selection). The instrumental response takes this selection into account. More detailed information about the instrument, its detection principle and performance can be found in Schönfelder et al. (1993).

4. Analysis methods

The measured event parameters $(\chi, \psi, \overline{\varphi}, E_{tot})$ constitute a 4-dimensional data space, in which we have to search for a "source signature". In practice the dimension of the data space is lowered by assuming a certain spectral shape for the sources to be searched for. The event distribution of a point source (the Point Spread Function (PSF)) in this reduced 3-d data space $(\chi, \psi, \overline{\varphi})$ is concentrated in a cone-shaped structure with its apex at the source position (χ_0, ψ_0). If the position of a (potential) source is *a priori* known it is also possible to determine the geometrical scatter angle φ_{geo} of an event from its scatter direction and the source direction. The difference angle (φ_{arm}) between $\overline{\varphi}$ and φ_{geo} is known as ARM (Angular Resolution Measure) angle and the ARM-distribution of events from a point source is characterized by a narrowly peaked distribution at $\varphi_{arm} = 0$. This ARM angle is used in the event selection procedures for timing analyses.

4.1. Timing analysis

4.1.1. Procedures and ephemerides

In the timing analysis the event arrival times at the spacecraft recorded with an intrinsic resolution of 0.125 ms are transformed to arrival times at the Solar System Barycentre (SSB) using the known instantaneous spacecraft position, the source position and the solar system ephemeris (JPL DE200 Solar System Ephemeris). The pulse phase ϕ is calculated from the following timing model:

$$\phi = \nu \cdot \Delta t + 1/2 \cdot \dot{\nu} \cdot \Delta t^2 + 1/6 \cdot \ddot{\nu} \cdot \Delta t^3 - \phi_0 \qquad (1)$$

In this formula Δt is given by $\Delta t = t^e - t^0$ with t^e the event SSB arrival time and t^0 the reference epoch. The values employed here for $t^0, \nu, \dot{\nu}, \ddot{\nu}, \phi_0$ are given in Table 2.

4.1.2. Detection significance of pulsed emission

The *modulation* significance i.e. the significance for a deviation from a statistically flat phase distribution is determined using the *bin free* Z_n^2-test statistic (Buccheri et al. 1983). The statistics behaves as a χ^2-distribution for $2n$ degrees of freedom (n=number of harmonics) in absence of any pulse signal, allowing the transformation from Z_n^2-test statistic to Gaussian sigma's. This test is rotation invariant what means that a shifted pulse-phase distribution would yield the same modulation significance. A problem is the number of harmonics to be used in the test, if the underlying pulse-shape is unknown. Narrowly peaked pulse-phase distributions for example require more harmonics in the test than distributions with broad modulation patterns. In the current COMPTEL timing analysis we constrained the number of harmonics in the test to 2 and 3 in view of our expectations based on the double peaked EGRET lightcurve observed for energies > 100 MeV.

4.2. Spatial and spectral analyses

For spatial point-source searches the events are first sorted in the 3-dimensional data space spanned by the 2-scatter directions (χ, ψ) and the calculated scatter angle $(\overline{\varphi})$ for a chosen measured energy interval. The search for the point source signature in this 3-d data space is performed by applying a maximum likelihood ratio (MLR) test at each scan position in the selected sky field of the instrument, rendering quantitative information on the source detection significance, position and flux (see de Boer et al. 1992). The ratio test is performed by maximizing the likelihood $\mathcal{L}^{H_0}$ (1 degree of freedom (dof)) under the zero hypothesis $\mathcal{H}_0$ i.e. a description of the data by a background distribution alone and maximizing the likelihood $\mathcal{L}^{H_1}$ (2 dof) under the alternative hypothesis $\mathcal{H}_1$ i.e. a data description in terms of a background model and a point source at the scan position. The quantity $Q = -2 \cdot ln(\mathcal{L}^{H_0(max)}/\mathcal{L}^{H_1(max)})$ is distributed as a χ_1^2 for 1 dof at each scan position. Mathematically we write the expectation value for pixel (i, j, k) under $\mathcal{H}_0$ as $\mu_{ijk}^{H_0} = \beta \cdot B_{ijk}$ with B_{ijk} the background estimate for pixel (i, j, k) and β a scale factor, and under $\mathcal{H}_1$ as $\mu_{ijk}^{H_1} = \sigma \cdot P_{ijk} + \beta \cdot B_{ijk}$ with P_{ijk} the source contribution in pixel (i, j, k) with strength σ. The

maximization process consists for e.g. the $\mathcal{H}_1$ case in finding the maximum of $\mathcal{L}^{H_1}(\sigma,\beta)$ given by:

$$\mathcal{L}^{H_1}(\sigma,\beta) = \prod_{ijk} \frac{\mu_{ijk}(\sigma,\beta)^{N_{ijk}} \cdot \exp(-\mu_{ijk}(\sigma,\beta))}{N_{ijk}!} \qquad (2)$$

with respect to both σ and β simultaneously. In this formula N_{ijk} represents the measured number of counts in pixel (i,j,k). From the optimized source scale factor $\sigma^{\max}$ and the exposure at the scan position it is possible to derive source fluxes and corresponding uncertainties (3-d likelihood method). The dominating (instrumental) background distribution in the 3-d dataspace ($\sim 95\%$ of the events passing through our selection filters are still mainly instrumental background events) has been determined from the data themselves using a smoothing method similar to that described in Bloemen et al. (1994). If the position of the source is *a priori* known we can also apply an equivalent likelihood analysis, but now in a 2-d space $(\varphi_{geo},\overline{\varphi})$ for each E_{tot} slice. This approach is in certain situations less sensitive to the background treatment, and is then particularly used for the generation of source spectra (2-d likelihood method).

In the case of a known timing signature, a third method can be applied to derive source flux information. This is based on the determination of the number of excess counts in an *a priori* chosen pulse-phase interval on top of a (flat) background level determined outside this pulse-phase interval in the lightcurve. The numbers of excess counts can be converted to flux values using the COMPTEL sensitivity to source events with measured ARM-values in the ARM-range applied in the event selection process for the timing analysis. It is important to note that the background estimates in the three methods are very different, in the latter case even completely independent from that in the spatial analyses, namely:

- The 3-d likelihood analysis for a chosen E_{tot} interval requires a background estimate for the full $(\chi,\psi,\overline{\varphi})$-dataspace.
- The 2-d likelihood analysis for a chosen E_{tot} interval requires a background estimate for the $(\varphi_{geo},\overline{\varphi})$-dataspace.
- In the case of a pulsar timing signature, a statistically flat part of the lightcurve is selected (or an interval known to be "empty" from results of other instruments) to determine the background level.

5. Timing analysis results

5.1. COMPTEL Event selections

The following event selections have been applied:

$0.07 < E1/1\,MeV < 20.0, 0.65 < E2/1\,MeV < 30.0, 113 < TOF < 130, 0 < PSD < 110$, EHA-$\overline{\varphi} > 0$, no VETO flag bits set and finally an additional ARM selection of $|\varphi_{arm}| \leq 3\overset{\circ}{.}5$. Except for the ARM selection the other event selections have also been applied in the spatial analysis. The applied ARM selection is in a narrow optimum range, as has been verified for the established MeV γ-ray pulsars Crab (Much et al 1995) and Vela (Kuiper et al. 1998).

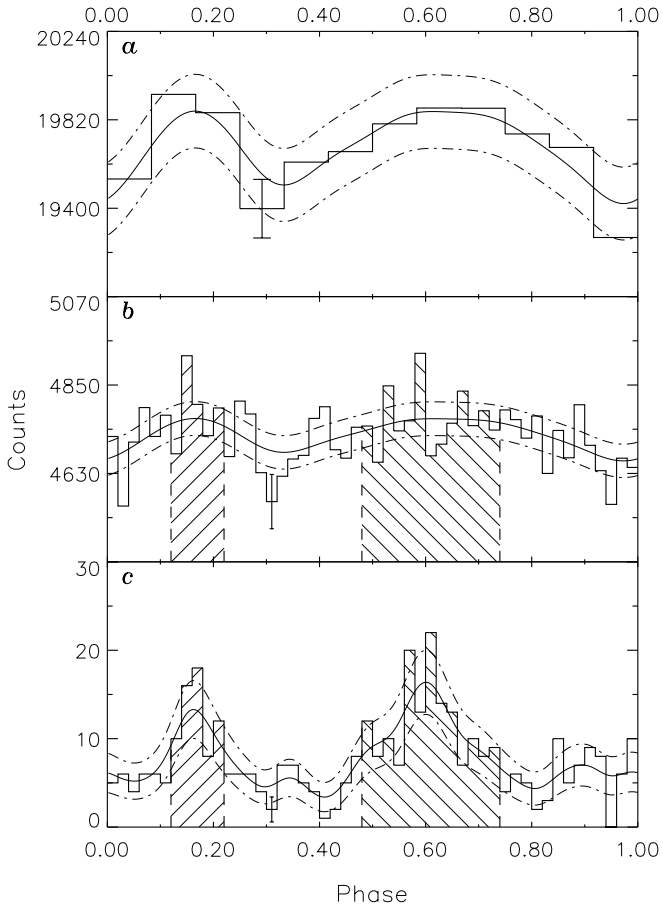

Fig. 1. a Radio-aligned 0.75-30 MeV 12-bin COMPTEL lightcurve for CGRO Cycle I data only (same data as used by Carramiñana et al. 1995). The KDE and its $\pm 2\sigma$ uncertainty range are superposed. **b** same as **a** but now with 50 bins. The shaded area corresponds to the "pulsed" definition introduced by Ramanamurthy et al. (1995) based on the EGRET > 100 MeV lightcurve. **c** EGRET 50 bin > 100 MeV lightcurve for the combination of the Cycle I, II and III viewing periods listed in Table 1. The KDE and its $\pm 2\sigma$ uncertainty range is superposed. The shaded area indicates the "pulsed" interval defined in Ramanamurthy et al. (1995). In all figures a typical 1σ error bar is indicated.

5.2. Consistency of COMPTEL and EGRET lightcurves

In order to be sure that the calculated pulse-phase (see Eq. 1) is compatible with the published EGRET lightcurve for energies above 100 MeV (Ramanamurthy et al. 1995), the first three entries of the set of ephemerides shown in Table 2 have first been used in a timing analysis of archival EGRET data (from VP 2.0 upto and including VP 333; see Table 1). Applying the same energy- and cone selections as in Ramanamurthy et al. (1995) we could reproduce the EGRET > 100 MeV lightcurve for the slightly enlarged combination of observations, demonstrating the consistent functioning of our timing analysis tools. The result is shown in Fig. 1c, in which phase 0.0 corresponds to the radio peak. Superimposed is also the Kernel Density Estimator (KDE; de Jager 1986) and its $\pm 2\sigma$ uncertainty range determined from the unbinned set of pulse-phases. This provides an (asymp-

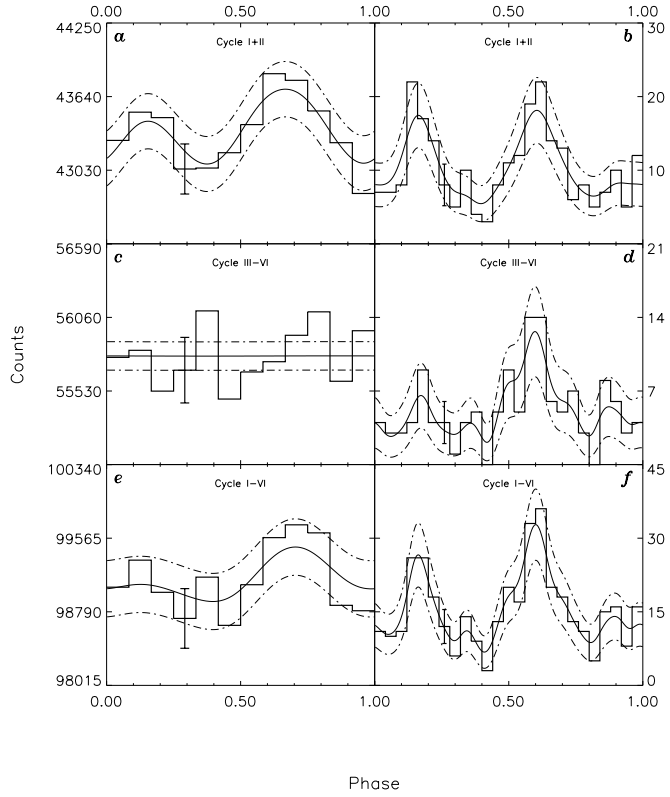

Fig. 2a–f. The pulse-phase distributions for COMPTEL (0.75-30 MeV; left panels **a,c,e** and EGRET ($>$ 100 MeV; right panels **b,d,f** shown for Cycles I+II and III-VI (comparable COMPTEL exposures), and the total (from top to bottom). In each frame the underlying unbiased estimate of the genuine pulse shape (KDE) is superposed as a solid line along with its $\pm 2\sigma$ uncertainty ranges (dashed-dotted lines). Typical 1σ error bars are indicated in each frame.

totically) unbiased view of the genuine underlying pulse-shape. The shaded areas indicate the "pulsed" interval defined by Ramanamurthy et al. (1995) as the combination of phase intervals 0.12-0.22 and 0.48-0.74 (P1+P2).

Next we repeated the analysis for the CGRO Cycle I COMPTEL data (i.e. data from VP 2.0, 7.0 and 20 combined) for which Carramiñana et al. (1995) found an indication for a narrow and a broad peak in the COMPTEL lightcurve at *unspecified* phases. The new radio-aligned COMPTEL lightcurve (see Fig. 1a for a 12 bin – and Fig. 1b for a 50 bin representation) for the total energy range 0.75-30 MeV shows two peaks co-aligned in phase with the peaks in the EGRET $>$ 100 MeV lightcurve. The Z_n^2-test statistic gives for 3 harmonics a modulation significance of 3.42σ (see Sect. 4.1.2). Superimposed in both Fig. 1a,b are the KDE and its $\pm 2\sigma$ uncertainty range, while typical 1σ errors are indicated. It is striking that the two highest bins in the COMPTEL 0.75-30 MeV lightcurve (Fig. 1b) coincide with the pulse maxima in the EGRET $>$ 100 MeV lightcurve (Fig. 1c). However, the significance of these two narrow peaks is too low to constrain significantly the KDE distribution.

5.3. Timing analysis for CGRO Cycles I–VI

The timing analysis has been performed using the data from all observations listed in Table 1. The derived *modulation* significances (see Sect. 4.1.2), irrespective of the peak locations in the lightcurve, for both the COMPTEL 0.75-30 MeV and contemporaneous $>$ 100 MeV EGRET pulse-phase distributions are shown in Table 3 for the individual CGRO Cycle VP combinations. Cycles IV-VI are combined to obtain an exposure comparable to the earlier Cycles. For COMPTEL also the excess counts in P1+P2 are listed. The same table lists these values for the combinations Cycle I+II, Cycle III-VI (comparable exposures) and the total I-VI. For the latter combinations the corresponding COMPTEL and EGRET lightcurves are shown in Fig. 2. The left panels (Fig. 2a,c,e) show the COMPTEL 0.75-30 MeV 12-bin lightcurves with superposed the KDE and its $\pm 2\sigma$ uncertainty range along with a typical 1σ error bar. The right panels (Fig. 2b,d,f) show the contemporaneous $>$ 100 MeV EGRET lightcurves.

As mentioned above, the *modulation* significance for the COMPTEL Cycle I 0.75-30 MeV pulse-phase distribution approaches/exceeds the 3σ level: 2.95σ for n=2 harmonics and 3.42σ for n=3 (see Table 3). However, the corresponding chance probability values of $3.2 \cdot 10^{-3}$ and $6.4 \cdot 10^{-4}$ for n=2,3 do not take into account that the observed lightcurve co-aligns with the EGRET lightcurve. This means that the detection significance of the pulsed signal with peaks at the expected positions is in fact higher. The increase in significance can be determined through simulations, which is the subject of the next section. Also, the modulation significance of the COMPTEL 0.75-30 MeV Cycle I+II pulse-phase distribution, approaching the 4σ-level, is a conservative estimate, and will be above the 4σ-level. Unfortunately, adding more COMPTEL data does not improve the detection significance further. No timing signal is seen for Cycles III-VI. The simulations described in the next section will address this problem as well. Spatial analysis, however, see also below, gives evidence that the source is present during all Cycles of the CGRO mission. The $\sim 4\sigma$-modulation significance of the 0.75-30 MeV Cycle I+II COMPTEL lightcurve with a double-peak pulse shape co-aligned with the EGRET lightcurve along with a point source in the maps (see below) consistent with the pulsars position led us already conclude that PSR B1951+32 was detected at MeV energies (Hermsen et al. 1997).

5.4. Lightcurve simulations

In order to study the effects of a weak pulsed signal atop of a dominating background distribution, we have now performed lightcurve simulations assuming a pulse-profile similar to the (KDE$-$KDE$_{min}$) of the EGRET $>$ 100 MeV Cycle I+II+III lightcurve (see Fig. 1c or equivalently Fig. 2f). The fraction of counts falling in the P1 and P2 intervals as defined by Ramanamurthy et al. (1995) is 0.67. For the background level definition used in the actual analysis, namely the average level in the phase intervals complementary to the P1 and P2 intervals, the fraction of pulsed "excess" counts is lower, namely 0.48. A typical simu-

Table 3. Modulation significances for PSR B1951+32 in COMPTEL and EGRET timing analyses, and the number of excess counts in the P1 and P2 phase intervals (see text) for different combinations of CGRO Cycles.

CGRO Cycle combination	n	COMPTEL $0.75-30$ MeV Sign.	COMPTEL $0.75-30$ MeV Excess counts	EGRET >100 MeV Sign.
I	2	2.95σ	1220 ± 295	2.32σ
	3	3.42σ		2.85σ
II	2	2.06σ	591 ± 321	4.05σ
	3	1.72σ		3.96σ
III	2	1.56σ	-545 ± 327	3.77σ
	3	1.81σ		4.32σ
IV-VI	2	0.05σ	-160 ± 367	—
	3	0.49σ		—
I+II	2	3.86σ	1813 ± 437	5.06σ
	3	3.52σ		5.45σ
III-VI	2	0.52σ	-705 ± 494	3.77σ
	3	0.76σ		4.32σ
I-VI	2	2.20σ	1109 ± 660	6.36σ
	3	1.78σ		7.23σ

lation consists in generating a background sample drawn from a uniform distribution and simulations of the pulsed signal drawing from the above described profile with a varying number of total pulsed counts. In the first set of simulations we have performed 6500 simulations for the case that we have not added a pulsed signal to the background sample (i.e. for the verification of the modulation significance determination) for a total number of counts of 235000, i.e. approximately the background level in the COMPTEL 0.75-30 MeV Cycle I pulse-phase distribution (see Fig. 1a, b) and $1500, 1000$ and 1000 simulations adding, respectively, sources for the following number of pulsed excess counts in P1+P2: $350, 700$ and 1065 (i.e. approaching the number of excess counts in P1+P2 (=1220) as measured in the COMPTEL 0.75-30 MeV Cycle I lightcurve). For each simulation we have determined the modulation significance as the Z_3^2-statistics value transformed to Gaussian sigmas and the *measured* number of excess counts in P1+P2 (N_E) using the complement of the P1+P2 phase interval as background interval.

The results of these simulations are shown in Fig. 3 for the different numbers of pulsed counts simulated in P1+P2. Along the x-axis the modulation significance is shown, and along the y-axis the number of excess counts in P1+P2 is given. The contour levels connect bins with the same probability level of occurence. Fig. 3 shows that in the presence of a pulsed signal the 2-d distributions become slanted indicating a correlation between the modulation significance and the number of excess counts measured in P1+P2. The centroids of the distributions, all intersected by the line specifying the number of simulated pulsed excess counts in P1+P2, shift towards higher Z_3^2 values the higher the number of pulsed counts put in P1+P2. From these 2-d distributions several important integral properties can be derived.

(i) For the background simulations (see Fig. 3 upper-left frame) the integral distribution of the Z_3^2 values (expressed in Gaussian sigmas; see Fig. 4) behaves, irrespective of the number of measured excess counts in P1 and P2, as the complementary error function, indicating that our modulation significance estimations have the *proper* calibration. We also showed this to be true when we used background samples from real flight data (Carramiñana et al. 1995).

(ii) In Fig. 5 (left panel) the Z_3^2-distributions are shown for the background simulations (shaded) and for the simulations with 1065 excess counts in P1+P2 atop of the background (grey). Note the shift of the distribution maximum towards $Z_3^2 \sim 2.5\sigma$ for the latter case. In the right panel of Fig. 5 distributions of the excess counts are shown for the same simulations. Gaussian fits to each of the distributions are superimposed. The peak widths (σ) are of the order of ~ 375 counts indicating that the spread is completely dominated by background fluctuations. The probability to detect a source with a pulse profile as measured by EGRET with 1065 excess counts (total number of pulsed counts in the profile ~ 2200) with a significance above 3.5σ is similar to the probability to obtain a significance below 1.5σ. Therefore, a source with flux close to our detection threshold will predominantly be detected when its signal is enhanced by a constructive background fluctuation. Consequently, in most cases the best estimate for its flux will be too high.

(iii) In the previous section we reported a negative result for our Cycle III - VI observations. We investigated this as follows: The normalized 2-d distributions (Fig. 3) for a given number of background counts B and pulsed excess counts C_E simulated in P1+P2 can be specified by $F(\zeta, \epsilon | B, C_E)$, where ζ refers to the $Z_3^2(\sigma)$ variable and ϵ to the N_E variable. Then the probability of measuring a negative number for the excess counts in P1+P2 irrespective of the Z_3^2-value is given by:

$$P(N_E < 0 | B, C_E) = \int_{-\infty}^{0} \int_{-\infty}^{\infty} F(\zeta, \epsilon | B, C_E) \cdot d\zeta \cdot d\epsilon \qquad (3)$$

The results are summarized in Table 4. The columns include the number of simulated pulsed excess counts put in P1+P2 (C_E), the number of background counts (B), Z_3^2 value in Gaussian sigma at the centroid (ζ_C, the maximum), the measured number of excess counts in P1+P2 (N_E) at the centroid N_{E_C}, the standard deviation of the measured excess counts distribution W_{E_C} and finally the probability $P(N_E < 0 | B, C_E)$ of measuring a negative number of excess counts in P1+P2 for a given background B and pulsed excess counts C_E simulated in P1+P2.

(iv) Finally, we would like to learn from the simulations the overall probability to measure a certain modulation probability and in addition a certain number of excess counts in a predefined phase window. In our case: What is the probability that random excesses in the COMPTEL phase distribution coincide with the

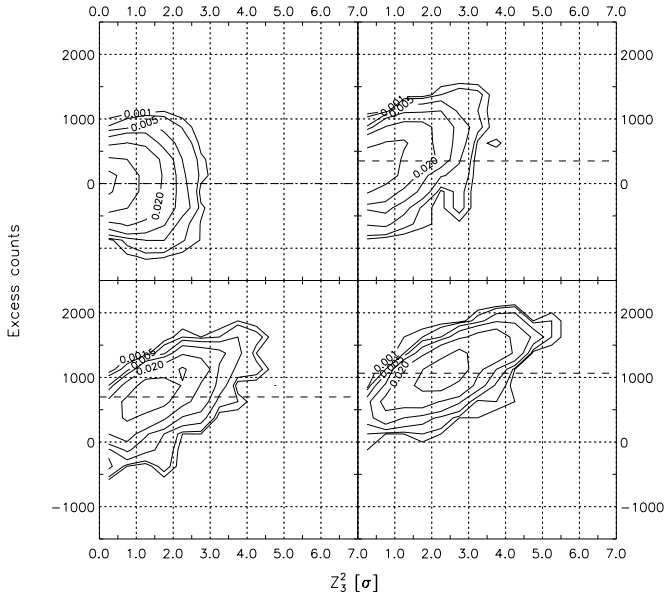

Fig. 3. Contour representation of lightcurve simulation results for different numbers of pulsed excess counts in the phase intervals 0.12-0.22 (P1) and 0.48-0.74 (P2) assuming an EGRET like pulse-phase distribution (used EGRET KDE of Fig. 2a–f) in a COMPTEL representative background environment with 235000 counts. *a*) (upper-left) 6500 pure backgound simulations; *b*) (upper-right) Adding source with 350 pulsed excess counts: 1500 simulations: *c*) (bottom left) Adding 700 pulsed excess counts: 1000 simulations. *d*) (bottom right) Adding 1065 pulsed excess counts: 1000 simulations. Dashed horizontal lines indicate the numbers of simulated pulsed excess counts in P1+P2.

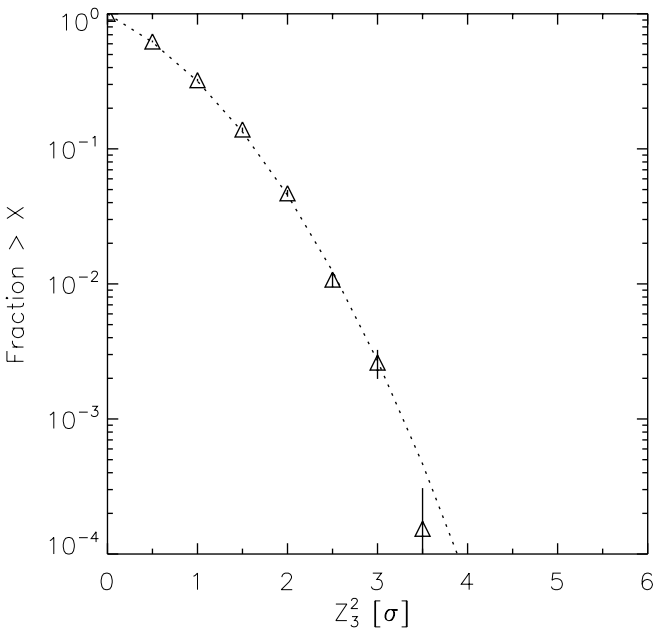

Fig. 4. The cumulative distribution of $Z_3^2(\sigma)$ for the 6500 background simulations. The triangles and error bars indicate the simulation results, while the dotted line represents the complementary error function - the expected functional shape of the cumulative distribution for lightcurve simulations of pure background.

Table 4. Global simulation results (see text)

C_E	B	ζ_C	N_{E_C}	W_{E_C}	$P(N_E < 0\|B, C_E)$
0	235000	0.81σ	-7	371	0.500 ± 0.009
350	235000	1.00σ	349	376	0.166 ± 0.011
700	235000	1.60σ	716	379	0.035 ± 0.006
1065	235000	2.42σ	1085	355	0.001 ± 0.001
0	470000	0.79σ	-12	507	0.503 ± 0.015
700	470000	1.16σ	684	510	0.089 ± 0.008
1050	470000	1.57σ	1024	521	0.022 ± 0.005
1400	470000	2.18σ	1380	536	0.005 ± 0.002

pulses in the EGRET light curve. From $F(\zeta, \epsilon|B, C_E)$ we can calculate the following 2-d integral:

$$\mathcal{F}(\zeta_l, \zeta_u, \epsilon_l, \epsilon_u|B, C_E) = \int_{\zeta_l}^{\zeta_u}\int_{\epsilon_l}^{\epsilon_u} F(\zeta', \epsilon'|B, C_E) \cdot d\zeta' \cdot d\epsilon' \quad (4)$$

and also the efficiency $\eta(\zeta_l, \epsilon_l|B, C_E)$ defined as:

$$\eta(\zeta_l, \epsilon_l|B, C_E) = \frac{\mathcal{F}(\zeta_l, \infty, \epsilon_l, \infty|B, C_E)}{\mathcal{F}(\zeta_l, \infty, -\infty, \infty|B, C_E)} \quad (5)$$

The quantity $\mathcal{F}(\zeta_l, \infty, -\infty, \infty|B, C_E)$ specifies the probability that we measure a modulation significance larger than ζ_l irrespective the number of measured excess counts in P1+P2 for given background B and pulsed excess counts C_E simulated in P1+P2. The efficiency $\eta(\zeta_l, \epsilon_l|B, C_E)$ specifies the fraction of $\mathcal{F}(\zeta_l, \infty, -\infty, \infty|B, C_E)$ having *in addition* measured excess counts in P1+P2 larger than ϵ_l. For the background simulations (see Table 5 upper 9 rows) it turns out that this factor ranges from 0.05 to 0.12 demanding a measured number of excess counts larger than 800. This means that the chance probability of measuring a $n \cdot \sigma$ modulation significance along with the restriction of measuring more than 800 excess counts in P1+P2 decreases by this factor; the *detection* significance of the pulsed signal typically increases $0.6 - 1.0\sigma$ with respect to the modulation significance. As a result the detection significance of the 0.75-30 MeV COMPTEL Cycle I lightcurve showing a modulation significance of 3.4σ with ~ 1200 excess counts in P1+P2 is $\gtrsim 4.1\sigma$ ($6.7 \cdot 10^{-5}$ chance probability). For the COMPTEL Cycle I+II 0.75-30 MeV lightcurve (see simulation summary in Table 6) the significance becomes also above 4.1σ for 3 harmonics and $\gtrsim 4.5\sigma$ for 2 harmonics, justifying our earlier claim of detection of pulsed emission from PSR B1951+32 at MeV energies.

As noted before, the genuine number of pulsed counts in P1+P2 in the 0.75-30 MeV range for Cycle I/I+II can, however, be overestimated in case of a constructive background fluctuation. The non-detection of the pulsed signal in the 0.75-30 MeV range during Cycle III - VI, having a comparable exposure of the pulsar as during Cycle I+II, points in that direction. If the genuine number of pulsed counts in P1+P2 is ~ 950 on top of 470000 background counts (representative number in the timing analysis for COMPTEL 0.75-30 MeV Cycle I+II and Cycle III - VI,

Table 5. Simulation results: : background level representative for COMPTEL energy range 0.75-30 MeV in timing analyses of Cycle I, II and III and Cycle IV - VI viewing period combinations

C_E	B	ζ_l	ϵ_l	$\mathcal{F}(\zeta_l,\infty,-\infty,\infty\|B,C_E)$ / $\eta(\zeta_l,\epsilon_l\|B,C_E)$	
0	235000	2.0σ	800	0.0469	0.049
0	235000	2.0σ	1000	0.0469	0.026
0	235000	2.0σ	1200	0.0469	0.010
0	235000	2.5σ	800	0.0108	0.114
0	235000	2.5σ	1000	0.0108	0.085
0	235000	2.5σ	1200	0.0108	0.043
0	235000	3.0σ	800	0.0026	0.058
0	235000	3.0σ	1000	0.0026	0.000
0	235000	3.0σ	1200	0.0026	0.000
350	235000	2.5σ	800	0.0480	0.458
350	235000	2.5σ	1000	0.0480	0.250
350	235000	2.5σ	1200	0.0480	0.139
350	235000	3.0σ	800	0.0100	0.667
350	235000	3.0σ	1000	0.0100	0.467
350	235000	3.0σ	1200	0.0100	0.267
700	235000	2.5σ	800	0.1510	0.795
700	235000	2.5σ	1000	0.1510	0.629
700	235000	2.5σ	1200	0.1510	0.371
700	235000	3.0σ	800	0.0630	0.921
700	235000	3.0σ	1000	0.0630	0.762
700	235000	3.0σ	1200	0.0630	0.540
1065	235000	2.5σ	800	0.4590	0.959
1065	235000	2.5σ	1000	0.4590	0.839
1065	235000	2.5σ	1200	0.4590	0.654
1065	235000	3.0σ	800	0.2540	0.976
1065	235000	3.0σ	1000	0.2540	0.909
1065	235000	3.0σ	1200	0.2540	0.811

Table 6. Simulation results for a background level representative for the COMPTEL energy range 0.75-30 MeV in timing analyses of Cycle I+II and in Cycle III - VI viewing period combinations

C_E	B	ζ_l	ϵ_l	$\mathcal{F}(\zeta_l,\infty,-\infty,\infty\|B,C_E)$ / $\eta(\zeta_l,\epsilon_l\|B,C_E)$	
0	470000	2.0σ	800	0.0418	0.096
0	470000	2.0σ	1000	0.0418	0.050
0	470000	2.0σ	1200	0.0418	0.042
0	470000	2.0σ	1400	0.0418	0.011
0	470000	2.5σ	800	0.0124	0.107
0	470000	2.5σ	1000	0.0124	0.036
0	470000	2.5σ	1200	0.0124	0.036
0	470000	2.5σ	1400	0.0124	0.036
0	470000	3.0σ	800	0.0022	0.200
0	470000	3.0σ	1000	0.0022	0.200
0	470000	3.0σ	1200	0.0022	0.200
0	470000	3.0σ	1400	0.0022	0.200
700	470000	3.0σ	800	0.0207	0.806
700	470000	3.0σ	1000	0.0207	0.710
700	470000	3.0σ	1200	0.0207	0.645
700	470000	3.0σ	1400	0.0207	0.484
700	470000	3.5σ	800	0.0060	0.556
700	470000	3.5σ	1000	0.0060	0.556
700	470000	3.5σ	1200	0.0060	0.444
700	470000	3.5σ	1400	0.0060	0.444
1400	470000	3.0σ	800	0.2010	1.000
1400	470000	3.0σ	1000	0.2010	0.990
1400	470000	3.0σ	1200	0.2010	0.970
1400	470000	3.0σ	1400	0.2010	0.920
1400	470000	3.5σ	800	0.0950	1.000
1400	470000	3.5σ	1000	0.0950	0.989
1400	470000	3.5σ	1200	0.0950	0.979
1400	470000	3.5σ	1400	0.0950	0.958

respectively) then the simulation results demonstrate that the detection of a pulsed signal (1800 counts) in the Cycle I+II data and the non-detection (-700 counts) in Cycle III - VI require statistical fluctuations in the dominating background of less than 3σ.

In summary the simulations demonstrate that:

- the pulsed signal in the COMPTEL 0.75-30 MeV range is detected at a $\gtrsim 4.1\sigma$ significance level (2 harmonics) with 1813 ± 437 excess counts for the combined Cycle I+II data.
- for an underlying background of 470000 counts there is a reasonable chance for a non-detection following this signal detection, if the genuine number of pulsed counts in P1+P2 is ~ 950. Namely, a statistical fluctuation $\lesssim 2\sigma$ is required in order to measure a negative signal, and $\lesssim 3\sigma$ to reach as low as -700 counts.
- an alternative explanation is the detection of a time variable signal. However, the steady behaviour in the EGRET window of PSR B1951+32 as well as the other known γ-ray pulsars makes this interpretation less likely.

6. Spatial- and spectral analysis

6.1. Spatial analysis

The spatial analysis at MeV energies of the sky region around PSR B1951+32 is complicated by the proximity of the black-hole X-ray binary Cyg X-1 at position (*l,b*) $= (71.^\circ34, 3.^\circ07)$ and at an angular distance of merely $\sim 2.^\circ6$ (cf. spatial resolution of COMPTEL is $\sim 1^\circ$), preventing the resolution of both sources spatially. Previous COMPTEL studies of Cyg X-1 using data from Cycle I, II and III by Van Dijk (1996) and McConnell et al. (1997) showed that Cyg X-1 dominates the COMPTEL sky maps for energies below 3 MeV. Above 3 MeV the situation was less clear. A weak source feature was evident in the combined CGRO Cycle I, II and III data, statistically consistent with the location of Cygnus X-1. However, the centroid of this feature was seen to be consistently offset from the exact location of Cygnus X-1 in the direction of the pulsar location. The shift of the excess going from the 1-3 MeV range to the 3-10 MeV range is nicely illustrated in the upper panel of Fig. 6 showing MLR maps for the 1-3 MeV and 3-10 MeV energy ranges of the Cygnus region (Cyg X-1 and PSR B1951+32 indicated by $+$

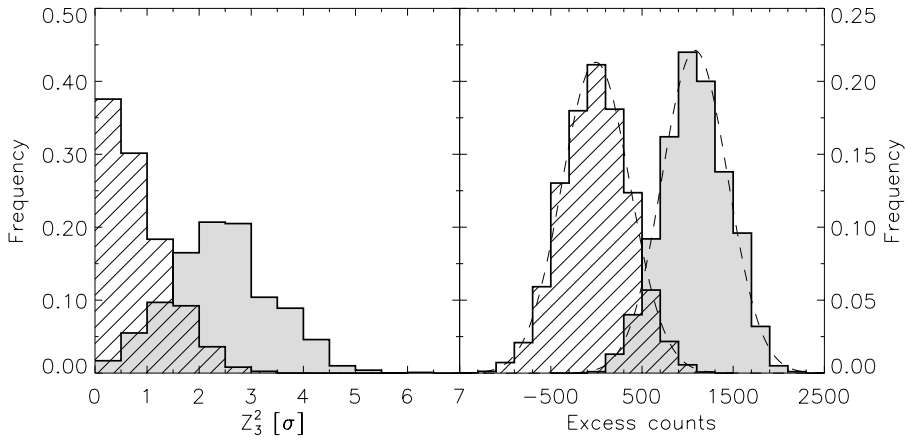

Fig. 5. Z_3^2 (left panel) and excess counts (right panel) distributions for two cases: background simulations (shaded) and simulations of 1065 pulsed counts put in P1+P2 atop a simulated background (grey).

and $\times$ signs, respectively) using all available COMPTEL data. This changing spatial morphology at MeV energies can be explained by a soft γ-ray source (Cyg X-1) located close to a hard γ-ray source (PSR B1951+32). The excess in the 3-10 MeV Cycle I - VI MLR map can be explained by the presence of the pulsar only. An explanation in terms of emission by Cyg X-1 only is less adequate leaving a strong ($\gtrsim 4.5\sigma$ for 1 dof) excess at lower longitudes near the pulsar position. This makes the pulsar the most likely candidate, but contributions from Cyg X-1 and other weak unidentified sources and/or emission of galactic diffuse origin with unknown spatial- and spectral distributions are likely. Analysing individually the Cycle I+II and Cycle III - VI datasets, which have similar exposures, indicates that this shift with energy persists over all Cycles (see Fig. 6 middle and bottom panel). In the 3-10 MeV MLR map for Cycle III - VI (bottom right plot of Fig. 6) a local maximum consistent with the Cyg X-1 position is visible. A spatial analysis (3-d - and 2-d maximum likelihood methods) selecting events from the pulsed (P1+P2) and unpulsed (complement of P1+P2) phase intervals was applied by Hermsen et al. (1997) using Cycle I+II+III data. This yielded in the "pulsed" maps for the 0.75-10 MeV range a $\sim 3.3\sigma$ excess at the pulsar position on top of Cyg X-1 - and diffuse galactic emission (assumed to be spatially distributed as H I and CO), while no excess was apparent in the "unpulsed" map. This combined timing and spatial analysis was performed particularly to derive flux information, but has been abandonned in this work. The above mentioned complicating factors – particularly the nearby strong time-variable source Cyg X-1 and the uncertain spatial- and spectral distribution of the emission of galactic diffuse origin – make the MLR map interpretation ambiguous. However, we have verified that at least the flux derived from the timing analysis (see below) is consistent with the flux derived from the 3-d - and 2-d spatial analyses.

6.2. Spectral analysis

In this work the flux information for PSR B1951+32 has been obtained from the determination of the excess counts in P1+P2 in the lightcurve (see Sect. 4.2), because in the phase-space all the complicating source components in the spatial analysis manifest themselves as statistically flat distributions. The disadvantage of this method, however, is that possible pulsed emission in the *a priori* defined unpulsed (here the EGRET definition was used) phase interval might raise the background level leading to an underestimation of the genuine pulsed flux. This cannot be ruled out in view of the observed changing spectral behaviour as a function of pulse-phase for e.g. the Crab, Vela and Geminga pulsars (Fierro 1995). Furthermore, DC-flux information can not be obtained by this method: this can only be determined through spatial analysis.

The source signature in the total dataset has become too weak to divide the total energy range in smaller energy bins. Therefore, we have used the 0.75-30 MeV Cycle I - VI lightcurve (see Fig. 2e) to derive our best estimate for the time-averaged pulsed 0.75-30 MeV flux from PSR B1951+32: $(7.7 \pm 4.6) \times 10^{-7}\ ph/cm^2 \cdot s \cdot MeV$. This flux will increase when we select a wider pulsed phase interval, but then the phase selection is not identical to the EGRET definition. In addition, the systematic uncertainty in the overall COMPTEL sensitivity could be up to $\sim 25\%$. In a broader high-energy spectral perspective the COMPTEL flux point is shown in Fig. 7, where also spectral information from other high-energy missions has been included: EGRET (Fierro 1995), OSSE (Schroeder et al. 1995), BATSE (Wilson et al. 1992) and RXTE (Chang et al. 1997).

7. Summary and discussion

The detection of a pulsed signal from PSR B1951+32 by COMPTEL can only be claimed based on earlier-mission data. Assuming that the MeV-emission from PSR B1951+32 is not time-variable, the COMPTEL detection of this pulsar in the data of CGRO-mission Cycles I and II (Hermsen et al. 1997) at a significance level $\gtrsim 4.1\sigma$ was fortunately high. The pulsar phase distribution exhibits two peaks, which are aligned in phase with the pulses measured by EGRET at high-energy γ-rays with a phase separation of ~ 0.44. The subsequent non-detection in data of Cycles III - VI indicates that the source flux has to be close to the COMPTEL detection threshold. The time-averaged (Cycle I+II+III) flux values which we published earlier (Hermsen et al. 1997) are slightly higher (by $\sim 1\sigma$) than the new single flux value presented in Fig. 7, including now also data from Cycle

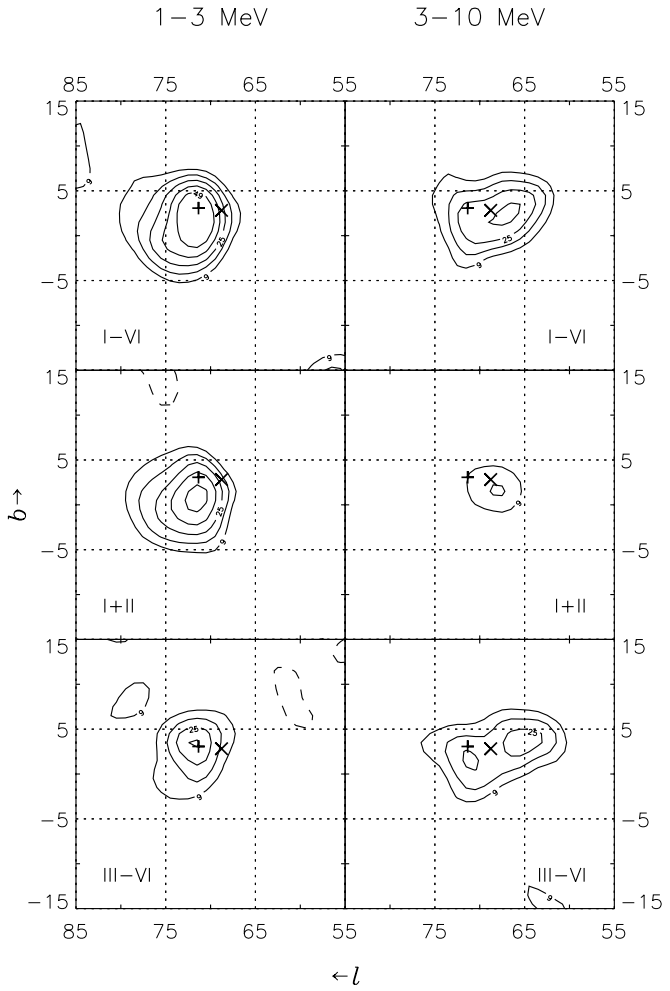

Fig. 6. MLR maps of the Cygnus region in two different energy intervals 1-3 MeV (left) and 3-10 MeV (right). From top to bottom are shown the maps for a combination of all data (upper panel; Cycle I - VI), for all Cycle I+II data (middle panel) and finally for all Cycle III - VI data (bottom panel). Contours starting at 3σ in steps of 1σ assuming 1 dof (corresponding maximum likelihood ratios are $9, 16, 25$, etc.). Dashed contours indicate regions with negative point source correlations (levels at $-9, -16$). The maps below 3 MeV are dominated by Cyg X-1 (+), while the excess shifts towards the PSR B1951+32 location ($\times$) for the 3-10 MeV energy window (see text).

IV - VI. This integral (0.75–30 MeV) flux is consistent with the EGRET spectrum measured above 50 MeV, but suggests a flattening w.r.t. the single-power-law best fit to the EGRET data (index -1.81 $\pm$ 0.09). The latter fit predicts 275 pulsed counts in the COMPTEL data for Cycle I+II, and 1813 ± 437 were detected. A single power-law fit to the phase-averaged EGRET data points and the phase-averaged time-averaged COMPTEL flux, covering a total energy range of 0.75 MeV to 30 GeV, changes indeed the index to -1.89 $\pm$ 0.07. The fit, see Fig. 7, is good with a reduced χ^2 of 0.46 and it is represented (in units $ph/cm^2 \cdot s \cdot MeV$) by :

$$F(E_\gamma) = (1.10 \pm 0.12) \cdot 10^{-10} \times (E_\gamma/423.64)^{(-1.89 \pm 0.07)}$$

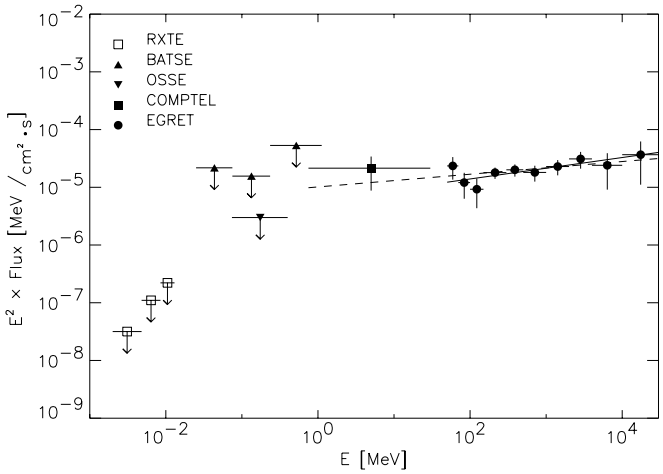

Fig. 7. Pulsed high-energy spectrum of PSR B1951+32 as observed by EGRET (Fierro, 1995), COMPTEL (this work), OSSE (Schroeder et al., 1995), BATSE (Wilson, 1992) and RXTE (Chang et al., 1997). The solid line shows the single power-law fit to the EGRET data points above 50 MeV; the dashed line the fit over the total COMPTEL and EGRET range.

Obviously, a substantial spectral break is required in the extrapolation to the X-ray domain to satisfy the OSSE and RXTE upper limits.

PSR B1951+32 is one of the four older (age $\gtrsim 10^5$ yr) radio pulsars detected at γ-ray wavelengths, namely: PSR B1951+32 (1.1×10^5 yr), PSR B0656+14 (also 1.1×10^5 yr; weaker detection in γ-rays, see Ramanamurthy et al. 1996, Hermsen et al. 1997), Geminga (3.4×10^5 yr) and PSR B1055-52 (5.3×10^5 yr). In this discussion we ignore the peculiar spectrum of PSR B0656+14 (which seems to have a narrow maximum in energy output in the range 10–30 MeV; Hermsen et al. 1997). In Fig. 7, it is apparent that the measured luminosity of PSR B1951+32 between roughly 1 and 30 MeV is comparable to the luminosity in a similar logarithmic energy interval in high-energy γ-rays. This contrasts the situation for the other older radio pulsars Geminga and PSR B1055-52. The latter pulsars are measured with (much) higher fluxes by EGRET above 100 MeV with spectral indices of -1.42 $\pm$ 0.02 and -1.59 $\pm$ 0.12, respectively (Fierro 1995), and no solid detections at COMPTEL energies could be reported sofar (for Geminga see Kuiper et al. 1996). In this respect PSR B1951+32 resembles more the younger pulsars Crab and Vela (indices above 50 MeV -2.12 $\pm$ 0.03 and -1.62 $\pm$ 0.01, respectively, Fierro 1995), although the total pulsar spectra of Crab and Vela differ significantly in their extrapolation to X-ray energies (see e.g. the review by Thompson et al. 1997). In fact, the spectral shape of PSR B1951+32 going from X-rays to γ-rays seems to have a shape rather similar to that of Vela. In this respect it is interesting to note that the efficiency in converting rotational energy loss into γ-rays (above 100 MeV) of PSR B1951+32 is $\sim 2 \times 10^{-3}$, roughly as efficient as the 10 times younger Vela pulsar. For the other older pulsars this efficiency is more than one order of magnitude higher.

Two types of models for pulsar γ-ray emission are discussed: Polar cap models (first proposed by Sturrock 1971; later extentions by Ruderman & Sutherland 1975; Harding 1981; Daugherty & Harding 1982; Arons 1983) and outer gap models (Cheng et al. 1986; Chiang & Romani 1992). The main difference between these scenarios is the region in which the γ-rays are produced. In the first this occurs in the vicinity of the star above the polar cap, in the latter, in vacuum gaps existing in the outer regions of the magnetosphere. In the most recent versions of these models a single pole picture is discussed, where the observer sees emission from one pole only. In polar cap models (Daugherty and Harding 1996; Sturner et al. 1995) the γ-ray emission beam is a hollow cone centered on the magnetic pole. In outer gap models (Romani & Yadigaroglu 1995; Romani 1996), the γ-ray emission is a wide, curved fan beam that is formed by the surface of the last open field line in the outer magnetosphere. Both types of models have successes and difficulties in explaining the variety of parameters which can be derived for the eight pulsars seen in γ-rays sofar. Below we will address only some points for which this COMPTEL detection of PSR B1951+32 has impact on the ongoing debate.

Daugerthy & Harding model γ-ray emission originating in extended polar gap cascades. These extended photon-pair cascades are initiated by curvature radiation from electrons accelerated above the polar cap. In order to reproduce satisfactorily the double-pulse Vela light curve and its spectrum with a high-energy cut-off around 3 GeV and the relatively high level of emission below 100 MeV, the acceleration of electrons above the polar cap had to start at a height of $\sim$1 neutron star radius above the neutron star surface and to extend up to several neutron star radii. Earlier models assumed that the acceleration to high energies takes place just above the surface of the neutron star. The total high-energy spectrum of PSR B1951+32 (Fig. 7) appears to have a higher energy cut-off compared to Vela's spectrum (around 10 GeV or higher) with also a relatively higher MeV flux. This spectrum is challenging the model even further.

In his most recent paper on radiation processes in the outer magnetosphere, Romani (1996) explains the low γ-ray efficiency above 100 MeV of PSR B1951+32 as being due to its low magnetic field, compared to the high magnetic fields and high efficiencies for Geminga and PSR B1055-52. Furthermore, his model identifies in the phase averaged spectrum a few components: A curvature radiation component dominating from $\sim$30 MeV to $\sim$10 GeV, a synchrotron component peaking at MeV energies, and at the extremes a thermal component at keV energies and Compton upscattering of the synchrotron spectrum on the primary $e^{\pm}$ at TeV energies. In order to explain the high COMPTEL flux below 30 MeV, an enhanced synchrotron contribution seems to be required. However, this cannot be reconciled with the low magnetic field of PSR B1951+32.

Zhang & Cheng (1997) discuss the γ-ray production in thick outer gaps. For older pulsars the outer gaps become larger, as pointed out by Ruderman & Cheng (1988). However, PSR B1951+32 appears to have a medium size gap (Vela type), smaller than the other post-Vela type pulsars PSR B0656+14, Geminga and PSR B1055-52. Zhang & Cheng (1997) show that the Vela spectrum (100 keV – 10 GeV) cannot be explained by their thick gap model, but that the available spectra for Geminga, PSR B1055-52 and PSR B1951+32 can. However, the spectrum shown in Fig. 7 with the new high COMPTEL flux is not consistent with their model spectrum, very similar to the Vela situation. For the latter they concluded that or the curvature radius of the top field line in the outer gap has to become larger, or that an explanation in terms of the thin outer gap model is required. This holds now also for PSR B1951+32.

Acknowledgements. The COMPTEL project is supported by NASA under contract NAS5-26645, by the Deutsche Agentur für Raumfahrtangelenheiten (DARA) under grant 50 QV90968 and by the Netherlands Organisation for Scientific Research (NWO). AC research is sponsored by the CONACYT grant 4142-E.

References

Angelini, L., White, N.E., Parmar, A.N., et al. 1988, ApJ 330, L43
Angerhofer, P.E., Strom, R.G., Velusamy, T., et al. 1981, A&A 94, 313
Arons, J. 1983, ApJ 266, 215
Bennett K., Buccheri, R., Busetta, M., et al. 1990, Proc. 21st ICRC, 1, 181
Bloemen H., Hermsen, W., Swanenburg, B.N., et al. 1994, ApJS 92, 419
Buccheri, R., Bennett, K., Bignami, G.F., et al. 1983, A&A 128, 245
de Boer, H., Bennett, K., Bloemen, H., et al., 1992, in: Data Analysis in Astronomy IV, Di Gesú, et al. (eds.). Plenum, New York, p. 241
Carramiñana, A., Bennett, K., Buccheri, R., et al. 1995, A&A 304, 258
Chang, H.-K., Ho, C. 1997, ApJ 479, L125
Cheng, L., Li, T., Sun, X., et al. 1994, Ap&SS 213, 135
Cheng, K.S., Ho, C., Ruderman, M.A. 1986, ApJ 300, 500
Chiang, J., Romani, R. 1992, ApJ 400, 629
Cordes J.M., Backer, D. C., Foster, R. S., et al. 1992, GRO/radio timing data base, Princeton University.
Daugherty, J.K., Harding, A.K. 1982, ApJ 252, 337
Daugherty, J.K., Harding, A.K. 1996, ApJ 458, 278
Fierro, J.M., 1995, Ph. D. thesis, Stanford University
Foster, R.S., Backer, D.C., Wolszczan, A., 1990, ApJ 356, 243
Foster, R.S., Lyne, A.G., Shemar, S.L., et al. 1994, AJ 108, 175
Fruchter, A.S., Taylor, J.H., Backer, D.C., et al. 1988, Nat 331, 53
Harding, A.K., 1981, ApJ 245, 267
Hermsen, W., Kuiper, L., Schönfelder, V., et al. 1997, in: The Transparant Universe, Winkler et al. (eds), ESA-SP-382, p. 287
de Jager, O.C., Swanepoel J.W.H., Raubenheimer B.C. 1986, A&A 170, 187
Kuiper, L., Hermsen, W., Bennett, K., et al. 1996, A&AS 120, C73
Kuiper, L., Hermsen, W., Schönfleder, V., et al. 1998, in: "The many faces of neutron stars", Buccheri et al. (eds), NATO ASI (in press)
Kulkarni, S.R., Clifton, T.C., Backer, D.C., et al. 1988, Nat 331, 50
Li, T., Li, J., Ma, Y., et al. 1990, Chin. Astron. Astrophys. 14, 10
McConnell, M., Bennett, K., Bloemen, H., et al. 1997, Proc. AIP conf., 410, 829, "Proceedings of the Fourth Compton Symposium", eds. C.D. Dermer, M.S. Strickman, and J.D.Kurfess
Much, R., Bennett, K., Buccheri, R., et al. 1995, A&A 299, 435
Ögelman, H., Buccheri, R., 1987, A&A 186, L17
Ramanamurthy, P.V., Bertsch, D.L., Dingus, B.L., et al. 1995, ApJ 447, L109
Ramanamurthy, P.V., Fichtel, C.E., Kniffen, D.A., et al., 1996, ApJ 458, 755

Romani, R.W. 1996, ApJ 470, 469
Romani, R.W., Yadigaroglu, I.A. 1995, ApJ 438, 314
Ruderman, M.A., Sutherland, P.G. 1975, ApJ 196, 51
Ruderman, M.A., Cheng, K.S., 1988, ApJ 335, 306
Safi-Harb, S., Ögelman, H., Finley, J.P., 1995, ApJ 439, 722
Schönfelder, V., Aarts, H., Bennett, K., et al., 1993, ApJS 86, 657
Schroeder, P.C., Ulmer, M.P., Matz, S.M., et al., 1995, ApJ 450, 784
Sturner, S.J., Dermer, C.D., Michel, F.C. 1995, ApJ 445, 736
Sturrock, P.A. 1971, ApJ 164, 529
Thompson, D.J., Harding, A.K., Hermsen, W., et al. 1997, Proc. AIP conf., 410, 39, “Proceedings of the Fourth Compton Symposium”, eds. C.D. Dermer, M.S. Strickman, and J.D. Kurfess
van Dijk, R., 1996, Ph. D. thesis, Univ. of Amsterdam
Wilson, R.B., Fishman, G.J., Finger, M.H., et al. 1992, Proc. AIP conf., 280, 291,”Compton Gamma-ray Observatory”, eds. M. Friedlander, N. Gehrels, and D.J. Macomb
Zhang, L., Cheng, K.S. 1997, ApJ 487, 370